

Electrodeposition-Potential Tuning Rejuvenates the Concurrent Preparation from α -Co(OH)₂ with Larger Interlayer-Spacings to β -Co(OH)₂

Xiangyu Wu,^[a] Meiqi Liu,^[a] Zhou Jiang,^[a] Jingjuan Li,^[a] Kexin Song,^[a] Aofei Wei,^[a] Detian Meng,^[a] Taowen Dong,^{*[a]} Zhenhai Gao,^[a] Wei Zhang,^{*[a]} and Weitao Zheng^{*[a]}

Electrodeposition is a popular method for preparing α -Co(OH)₂ as an electrode material for electrochemical energy storage. However, the preparation of technically important β -Co(OH)₂ through electrodeposition remains lacking thus far. Herein, we successfully prepared Co(OH)₂ in two phases, α - and β -Co(OH)₂, by simply adjusting the electrodeposition potentials, as evidenced by a package of microscopy and spectroscopy analysis. Benefited from a delicate embedding and sectioning technique that may inhibit the loss of interlayer water in microscopy analysis, we find the presence

of Co tetrahedron in the interlayer of α -Co(OH)₂ results in a large interlayer spacing of 7.2 Å for the crystal plane (003) compared to β -Co(OH)₂, as well as a higher chemical valence of cobalt in electrodeposited β -Co(OH)₂. The large interlayer spacing creates wider ion channels and more active storage sites for effective energy storage. Consequently, the α -Co(OH)₂ electrode exhibits more competitive electrochemical performance compared to its β counterpart.

1. Introduction

Co(OH)₂ has a high theoretical specific capacity 1886 Fg⁻¹, according to the equation $C_s = (n \times F) / (M \times V)$, where n is the number of transferred electrons ($n=1$), F is Faraday's constant, M is the molecular mass, and V is the potential window ($-0.1 - -0.45$ V).^[1] Moreover, it also exhibits a significant actual capacity due to the intrinsic bulk utilization of electrode material.^[1,2] Additionally, Co(OH)₂ is widely recognized for its excellent rate performance and cyclic stability, attributed to its stabilized layer structure that facilitates ion transport.^[3-5] Therefore, Co(OH)₂ is classified as the battery-type electrode for hybrid capacitors or even as a popularly pseudocapacitive electrode.^[6-8]

Co(OH)₂ has a typical layered structure and exists in two polymorphs, α - and β -Co(OH)₂.^[9] For the former, as shown in Figure 1a, it possesses both tetrahedrally and octahedrally coordinated Co. The Co-tetrahedra are located at the side of each slab, while anions (Cl⁻, NO₃⁻, etc.) coordinate with the tetrahedra or occupy the corridors to maintain charge neutrality.^[10] The presence of tetrahedra, anions, and water molecules leads to a large interlayer spacing (>7 Å) for α -

Co(OH)₂; the interlayer spacing can be modulated by the introduction of different anions.^[11] The electrochemical performance is significantly dependent on the interlayer spacing, as larger layer distances not only facilitate expansive ion transport pathways but also augment the utilization efficiency of the electrode material. However, so far, such large interlayer spacing in α -Co(OH)₂ has not been observed by transmission electron microscopy (TEM), a direct visualization technique for crystal structure in reciprocal space, real space, or energy space.^[12] For the latter of β -Co(OH)₂, as shown in Figure 1b, it features with only an octahedral structure. No anions or water molecules exist between the interlayers, resulting in a reduced interlayer spacing of 4.6 Å.

Co(OH)₂ can be prepared using several methods,^[13] including hydrothermal,^[14] solvothermal,^[15] co-precipitations,^[16] chemical vapor deposition,^[17] and sol-gel methods.^[18] Among these, electrodeposition is a popular method for preparing Co(OH)₂ as an electrode for electrochemical energy storage because it is free of binder and conductive agent.^[19,20] Bhosale and Fulari studied how electrodeposition potential and time affect the electrochemical performance of Co(OH)₂.^[21] Yarger et al. introduced surfactants into the interlayer to regulate the spacing during the electrodeposition process.^[22] Lévy-Clément et al. investigated the effects of electrodeposition temperature on the phase structure.^[23] However, as a critical parameter, the effect of electrodeposition potential on the phase of Co(OH)₂ has not yet been investigated.

As shown in Figure 1c, different ions exhibit a variety of interaction in an aqueous solution, particularly under different potentials. Therefore, it is of great interests to explore the possibility for the formation of different phases under varying electrodeposition potentials. Herein, we demonstrate the phase of Co(OH)₂ can be modulated from α - to β -Co(OH)₂ by adjusting the electrodeposition potential while keeping other parameters

[a] X. Wu, M. Liu, Z. Jiang, J. Li, K. Song, A. Wei, D. Meng, T. Dong, Z. Gao, W. Zhang, W. Zheng
National Key Laboratory of Automotive Chassis Integration and Bionics, and
School of Materials Science & Engineering, and
Key Laboratory of Automobile Materials MOE, and
Electron Microscopy Center, Jilin University, Changchun 130012, China
E-mail: twdong@jlu.edu.cn
weizhang@jlu.edu.cn
wtzheng@jlu.edu.cn

 Supporting information for this article is available on the WWW under
<https://doi.org/10.1002/batt.202400699>

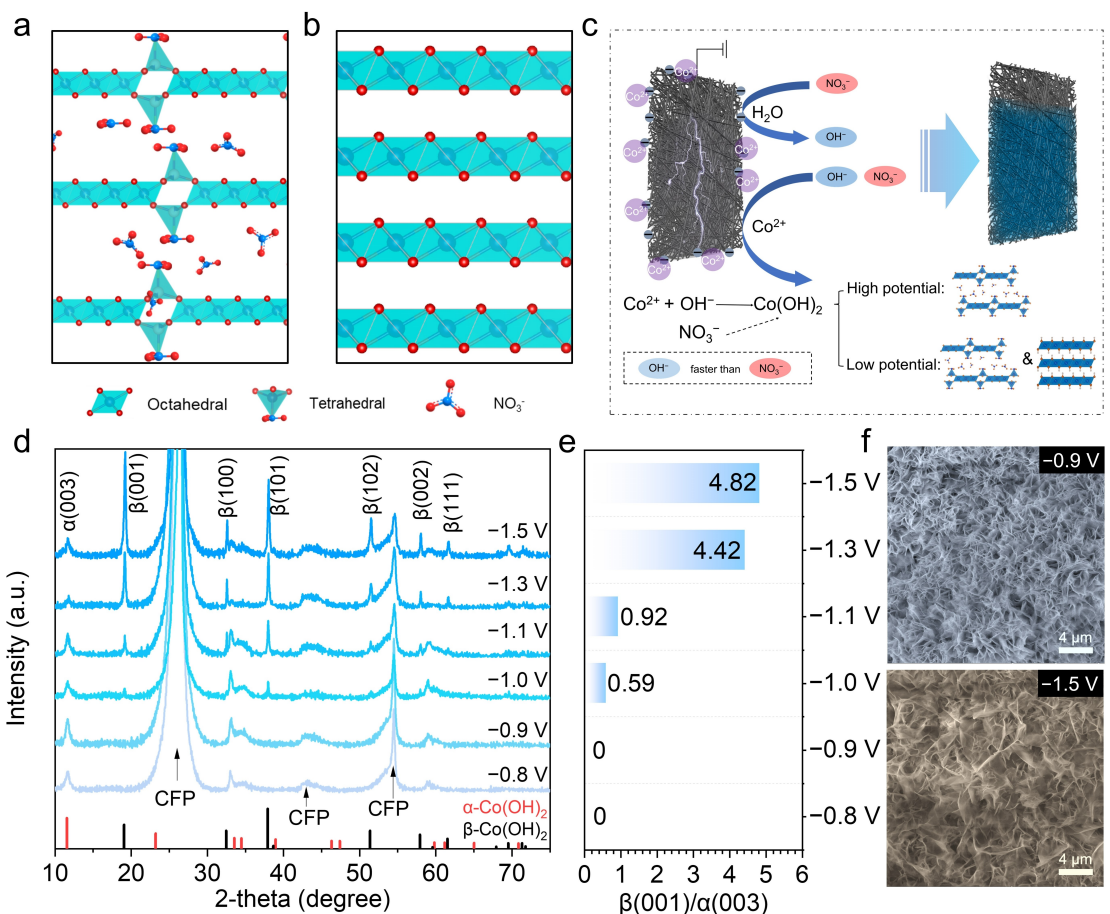


Figure 1. Electrodeposition Co(OH)₂ in two phases. a–b) Schematic structure of α- and β-Co(OH)₂, respectively (Green, Red and blue balls stand for cobalt, oxygen and nitrogen atoms, respectively). c) Schematic illustration of electrodeposition for α- and β-Co(OH)₂ in different potentials. d) XRD patterns of Co(OH)₂ electrodeposited at different potentials. e) Intensity ratios between (001) of β-Co(OH)₂ and (003) of α-Co(OH)₂. f) SEM images at different potentials.

constant. More importantly, to the best of our knowledge, the interplanar spacing of crystal plane (003) for α-Co(OH)₂ is determined for the first time to be 7.2 Å by using TEM. Our results not only propose a new strategy, i.e., tuning potential to modulate the phase of Co(OH)₂ prepared through electrodeposition, but also provide a visible evidence of the layered structure of α-Co(OH)₂.

2. Experimental Section

Materials and chemicals: The current collector used for the electrodeposition is carbon fiber paper (CFP), model TGP-H-060. CFP is washed in acetone, ethanol, and deionized water for 0.5 hours, respectively, after which it is placed in an oven with 60 °C for 6 hours. Cobalt nitrate hexahydrate (AR ≥ 98.5%, Sinopharm Chemical Reagent Co., Ltd) was selected to prepare the 0.1 M (7.28 g Co(NO₃)₂·6H₂O dissolved in 250 ml deionized water) solution for electrodeposition.

Synthesis: Electrodeposition was conducted in a three-electrode system, with a platinum electrode as the counter electrode, a mercuric oxide electrode as the reference electrode, and a CFP (1 cm×1.5 cm) as the working electrode. The electrochemical workstation is from IVIUM (Vertex, C). Electrochemical synthesis of cobalt hydroxide nanosheets by chrono-current method in a water bath at

a constant temperature of 45 °C. The electrochemical deposition process is as follows:^[24,25]



After electrodeposition, the samples were rinsed in deionized water for cleaning. Then, the samples are dried in an oven at 60 °C for 6 hours. Cobalt hydroxide mass can be measured by weighing the difference in CFP mass before and after electrodeposition.

3. Results and Discussion

Electrodeposition was conducted in the three-electrode electrochemical system using amperometric i-t mode. CFP (the morphology is shown in Figure S1), 0.1 M Co(NO₃)₂·6H₂O, and a temperature of 45 °C were selected as the current collector, solution, and electrodeposition temperature, respectively. In this work, we focus on the effect of electrodeposition potentials on the phase of Co(OH)₂. Thus, we conducted the electrodeposition in several potentials (-1.5 V, -1.3 V, -1.1 V, -1.0 V, -0.9 V, -0.8 V) while keeping other parameters constant. As

shown in Figure 1d, the X-ray diffraction (XRD) patterns indicate that as the potential is reduced from -0.8 to -1.5 V (vs saturated calomel electrode (SCE)), the phase evolves from $\alpha\text{-Co(OH)}_2$ (PDF#00-046-0605) to a coexistence of $\alpha\text{-Co(OH)}_2$ and $\beta\text{-Co(OH)}_2$ (PDF#00-043-0443). With decreasing the electrodeposition potentials, the intensity ratio between the peaks for the crystal planes (001) of $\beta\text{-Co(OH)}_2$ and (003) of $\alpha\text{-Co(OH)}_2$ increases (Figure 1e). This increase may originate from the growing mass of electrodeposited $\beta\text{-Co(OH)}_2$ and its crystallinity. Meanwhile, the prominent intensity at the (001) and (003) peaks for $\beta\text{-Co(OH)}_2$ and $\alpha\text{-Co(OH)}_2$, respectively, indicates the presence of preferred orientation in crystal growth during the electrodeposition process.^[26,27] From scanning electron microscopy (SEM) images (Figure 1f), the evolution of morphology is clearly observed. The Brunauer-Emmett-Teller (BET) method was employed to determine the specific surface areas of α - and $\beta\text{-Co(OH)}_2$ (Figure S2 for measurement details). The specific surface areas of α and β phases were determined to be 3.77 and $5.14 \text{ m}^2 \text{ g}^{-1}$, respectively. The BET results were in agreement with the SEM analysis.

The formation of $\beta\text{-Co(OH)}_2$ occurs as the potential decreases, the phenomenon is in perfect accord with electrochemical principles. The electrodeposition process is bifurcated into two stages: the generation of hydroxide ions (OH^-) on the surface of the working electrode, and the subsequent precipitation reaction with Co^{2+} ions (further details of this process are delineated in the Supporting Information). The production of OH^- ions is more abundant at lower potentials, a behavior that parallels the temperature-induced effects on the structural composition of the electrodeposited phase as observed by Vladimir Parra-Elizondo and colleagues.^[28] The anions swiftly migrate towards the electrode-electrolyte interface, where they precipitate with Co^{2+} ions under the influence of the electric field. Ion migration rates (v) of OH^- and NO_3^- are 20.52×10^{-8} and $7.40 \times 10^{-8} \text{ m}^2 \cdot \text{V}^{-1} \cdot \text{s}^{-1}$, respectively. According to the equation $J = \pm c \cdot v$, where J is the flux of ions, c is the concentration, and v is the migration rate proportional to the gradient in electrochemical potential, the difference in migration rates between these ions will be enlarged under the electric field as the electrodeposition potential decrease. This indicates that the OH^- ions engaged in the precipitation reaction exhibit a more accelerated reaction rate in contrast to nitrate ions (NO_3^-), with this effect being particularly accentuated at lower potentials. Consequently, the selective formation of α - and $\beta\text{-Co(OH)}_2$ in response to the speed of OH^- ions is a rational consequence of these electrochemical behaviors.^[29]

Morphology, microstructure and chemical characteristics of electrode materials are very critical to understand their electrochemical behaviors. Such information was collected to understand the discrepancy between the two typical electrodes electrodeposited at potentials of -0.9 V ($\alpha\text{-Co(OH)}_2$) and -1.5 V (α - and $\beta\text{-Co(OH)}_2$) by using TEM.

First, the morphology was studied. As shown in Figure 2a, d, $\alpha\text{-Co(OH)}_2$ exhibits a petal-like morphology, while a nano-hexagonal structure for $\beta\text{-Co(OH)}_2$. Figure 2b shows the electron diffraction for $\alpha\text{-Co(OH)}_2$, indicating the preferred crystallization along the specific crystal direction [001],^[25] which is in

accordance with the previous XRD analysis. Notably, one can notice that diffraction spots are elongated at an angle of $\Phi = 4.95^\circ$ ($< 10^\circ$), suggesting the existence of small angle grain boundaries.^[30,31] In addition, the presence of diffraction ring suggests the presence of polycrystalline regions, which is often favorable for electrochemical energy storage.^[32] Figure 2e shows the electron diffraction for electrode electrodeposited at potentials of -1.5 V, suggesting the occurrence of $\beta\text{-Co(OH)}_2$. In addition, the diffraction spots are not elongated, not as observed in electrodes electrodeposited at -0.9 V, indicating enhanced crystallinity, which is in high agreement with our XRD analysis.

Secondly, a high-resolution transmission electron microscope (HRTEM) was performed to examine the microstructure of the two samples. The HRTEM image of $\alpha\text{-Co(OH)}_2$ (Figure 2c) reveals three sets of lattice fringes with an interplanar spacing of 2.90 \AA , which are assigned to the (100), (1-10) and (0-10) planes along the [001] zone axis. Similarly, the HRTEM image of $\beta\text{-Co(OH)}_2$ (Figure 2f) also shows three sets of lattice fringes, with the interplanar spacing of 2.92 \AA , attributed to the (1-10), (0-10) and (-100) planes. One point should be noted that the actual interplanar spacing drift under electron beam irradiation compared to the theoretical values (Theoretically for $\beta\text{-Co(OH)}_2$, (100) the crystal plane spacing is 2.76 \AA and for $\alpha\text{-Co(OH)}_2$ (100) the crystal plane spacing is 2.67 \AA).

Lastly, similar to that discussed above, those reported images of the microstructure of Co(OH)_2 obtained by TEM are typically observed along the crystal direction [001].^[33-35] In contrast, the images showing the microstructure along the crystal direction $<100>$, which pertains to the interlayer structure, are scarce as challenging to obtain. In fact, capturing the interlayer microstructure is very beneficial not only for understanding the interlayer chemical circumstance but also for correlating it with the electrochemical performance. To address this issue, the embedding and sectioning techniques were delicately taken to prepare the sample for TEM measurements in this work. Such a preparation method offers two advantages: 1) it reduces the lattice shift due to electron beam irradiation, and 2) allows for observation of the HRTEM images at specific orientations. As shown in Figure 2g, for $\alpha\text{-Co(OH)}_2$, the lattice fringes are clearly visible, with a large interlayer spacing at 7.2 \AA , which corresponds perfectly to the crystal plane (003) of $\alpha\text{-Co(OH)}_2$. The intensity line profile (Figure 2i) reveals an additional layer (marked by red arrows), possibly arisen from the presence of Co tetrahedra. Additionally, the nanosheet exhibits lattice distortion (Figure S3). The analyzed nanosheets have a thickness of 11 nm , formed by the stacking of ~ 15 layers of $\alpha\text{-Co(OH)}_2$ slab. These ultra-thin nanosheets provide a larger specific surface area and more reaction sites for electrochemical reactions. In Figure S4, we performed energy dispersive X-ray spectroscopy (EDS) line scans of the interlayer elements, demonstrating the existence of cobalt, oxygen, and nitrogen elements in the layers. In contrast, Figure 2h shows $\beta\text{-Co(OH)}_2$, with an interlayer spacing of 4.6 \AA , which is well matched with the crystal plane (001) of $\beta\text{-Co(OH)}_2$. Distinguished from that in the $\alpha\text{-Co(OH)}_2$, no additional layer is found in the intensity line profile (Figure 2j) and the nanosheets remain compact and straight (Figure 2h and Figure S5). The analyzed nanosheets

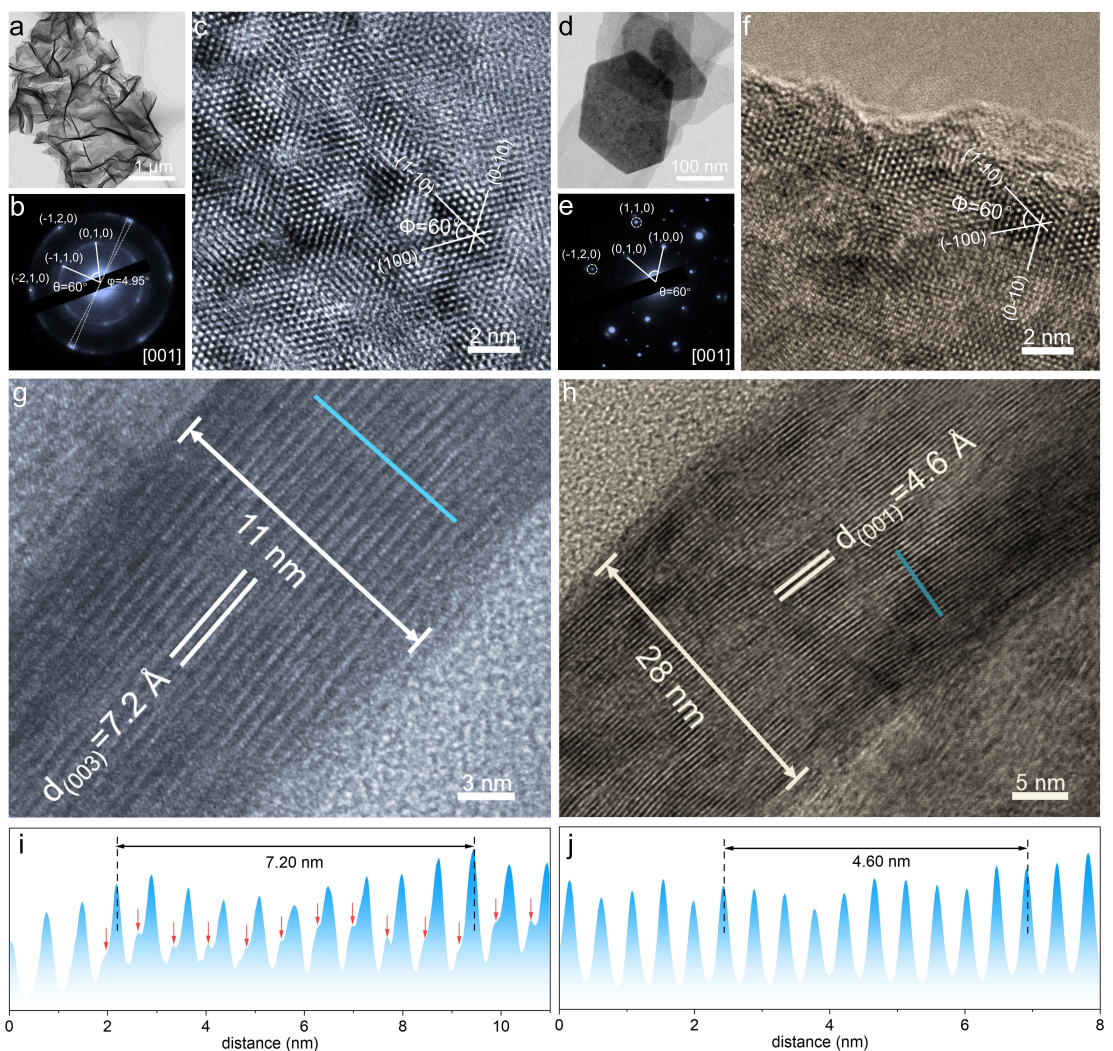


Figure 2. Structural characterization by using TEM. a) Morphology of the deposited sample at -0.9 V potential ($\alpha\text{-Co(OH}_2\text{)}$, b) and corresponding electron diffraction. c) HRTEM image of a -0.9 V electrodeposited sample. d) Morphology of the deposited sample at -1.5 V potential, e) and corresponding electron diffraction. f) HRTEM image of a -1.5 V electrodeposited sample. g) Cross-sectional HRTEM image of a -0.9 V electrodeposited sample, and i) corresponding the intensity line profile. h) Cross-sectional HRTEM image of a -1.5 V electrodeposited sample, and j) corresponding intensity line profile.

have a thickness of 28 nm, formed by the stacking of ~ 60 layers of $\beta\text{-Co(OH}_2\text{)}$ slab.

Furthermore, several spectroscopy characterization techniques were employed to examine the electronic structure and chemical composition of electrodeposited $\text{Co(OH}_2\text{)}$ at different potentials. The wavelength 513 nm and 547–670 nm are mainly the absorption spectrum of Co octahedron and tetrahedron in UV-visible diffuse reflectance spectra (UV-Vis DRS), respectively.^[10,36] As in Figure 3a, the characteristic peaks of the Co octahedron at 513 nm are gradually enhanced by decreasing the electrodeposition potential. While the absorption peaks of Co tetrahedron still exist. These data confirm the formation of $\beta\text{-Co(OH}_2\text{)}$ along with the decreasing electrodeposition potential. We simulated the 513 nm, 547 nm, and 670 nm peaks as color complements according to a Gaussian distribution superimposed at different intensities by a natural light mixing pattern. The simulated colors for samples electrodeposited at different potentials are shown in Figure 3b. Raman spectroscopy is shown in Figure 3c, these patterns include peaks at ~ 190 , 470,

510, and 675 cm^{-1} .^[37,38] The peak at 190 cm^{-1} is associated with symmetric bending of oxygen anions on tetrahedra and octahedra.^[39] Peaks at 470 cm^{-1} , 510 cm^{-1} , and 675 cm^{-1} are attributed to O–Co–O stretching vibration ($\gamma\text{ O–Co–O}$), Co–O stretching vibration ($\gamma\text{ Co–O}$), and Co–O–H bending vibration ($\delta\text{ Co–O–H}$), respectively. The observed shift of the Raman peak towards higher wavelengths as the deposition potential decreases can be attributed to the improved crystallinity and alignment of the $\text{Co(OH}_2\text{)}$ electrodeposited at reduced potentials.^[35] Fourier transform infrared spectroscopy (FT-IR) was also performed, as depicted in Figure 3d. Peaks at 1380 cm^{-1} and 1482 cm^{-1} correspond to the N–O₂ symmetric stretching vibration and the asymmetric stretching vibration in NO_3^- which is coordinated to Co in Co-tetrahedron (C_{2v} symmetry). The peak at 1059 cm^{-1} is attributed to an O–N antisymmetric stretching vibration for free NO_3^- (D_{3h} symmetry).^[40] The peaks at 3487 cm^{-1} and 3629 cm^{-1} are bending vibrations of O–H in water and in $\beta\text{-Co(OH}_2\text{)}$, respectively.^[41] Furthermore, X-ray photoelectron spectroscopy (XPS) was performed to investigate the

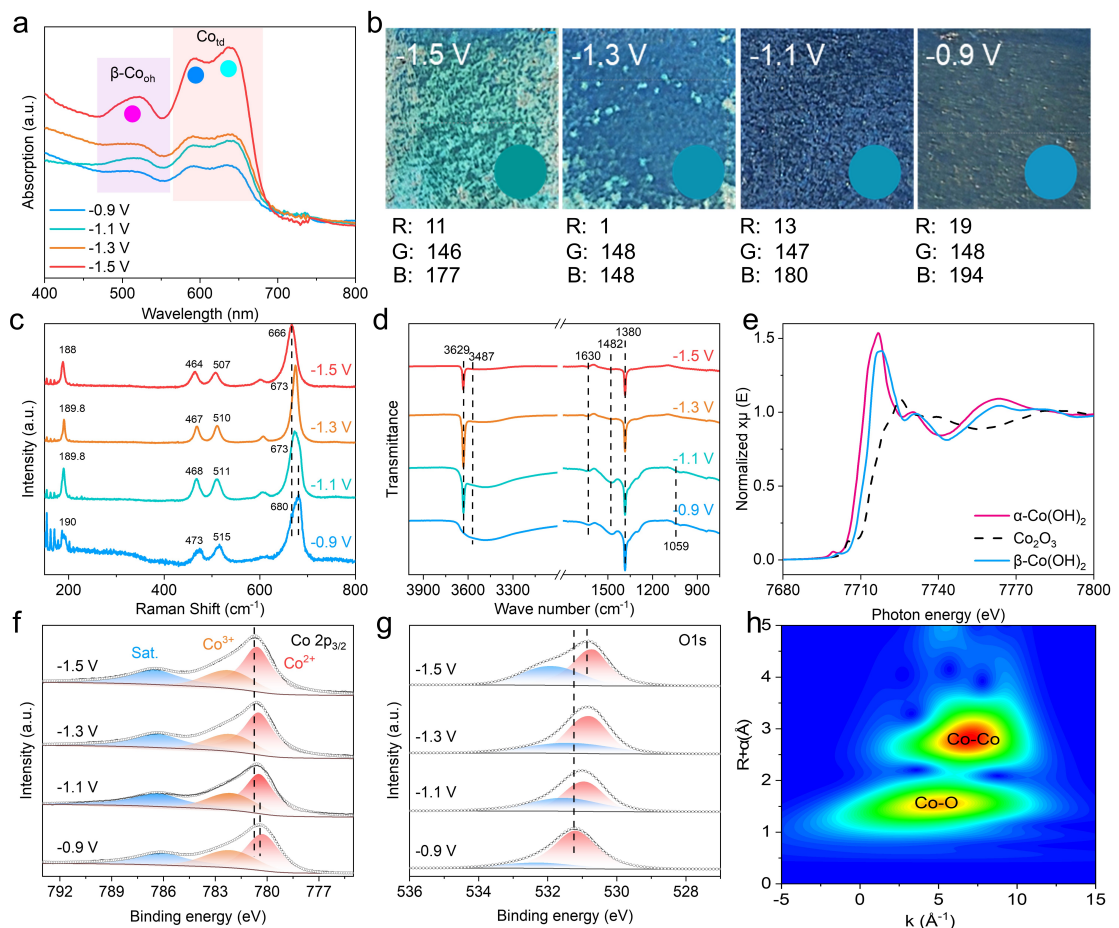


Figure 3. Spectroscopy characterization of electrodeposited $\text{Co}(\text{OH})_2$ at different potentials. a) UV-Vis DRS. b) Optical photographs of electrodeposited samples as well as RGB color simulation. c) Raman spectra. d) FT-IR. e) X-ray absorption spectra. f) XPS $\text{Co}2\text{p}_{3/2}$. g) XPS O1s. h) Wavelet transform of EXAFS for α - $\text{Co}(\text{OH})_2$.

chemical state and bonding state of electrodeposited $\text{Co}(\text{OH})_2$. The XPS survey spectra (Figure S6) show the presence of Co, O, and N elements, which is in accordance with the aforementioned EDS line scan analysis. As shown in Figure 3f, high-resolution XPS Co $2\text{p}_{3/2}$ spectra can be deconvoluted into two main peaks at 780.52 eV and 782.26 eV, corresponding to Co^{2+} and Co^{3+} , respectively, while the peak at 786.43 eV is typical satellite peak for Co^{2+} .^[42-44] Due to the different chemical environments of the two samples, the peaks at different potentials are shifted to a small extent.^[45,46] In the high-resolution O1s spectra (Figure 3g), the peaks located at 530.7 eV and 532 eV correspond to Co–O–Co and H–O–Co, respectively. For further investigating the chemical valence and the coordination state of $\text{Co}(\text{OH})_2$, the Co K edge was characterized by X-ray absorption spectroscopy (XAS).^[47] In Figure 3e, the valence states of Co are both lower than +3 for two samples, and the one in the β - $\text{Co}(\text{OH})_2$ is higher than the one in its α -counterpart. This conclusion is in agreement with the XPS analysis above.^[48] As shown in Figure 3h, the wavelet transform of the extend X-ray adsorption fine structure (EXAFS) spectrum shows the Co–Co and Co–O shells in α - $\text{Co}(\text{OH})_2$.

As illustrated in Figure 4a, there is a noticeable gradient in the specific capacity of $\text{Co}(\text{OH})_2$ electrodeposited at different potentials. The specific capacity of the sample prepared at -0.9 V (α - $\text{Co}(\text{OH})_2$)

is markedly higher than that of the sample prepared at -1.5 V (predominantly β - $\text{Co}(\text{OH})_2$). The electrochemical performance of these two typical samples was studied in more detail. Figure 4d, g show the cyclic voltammetry (CV) curves of $\text{Co}(\text{OH})_2$ electrodeposited at -0.9 V and -1.5 V, respectively, at scanning rates of 5, 10, 25, 50 mVs⁻¹. Obviously, the CV curves of α - $\text{Co}(\text{OH})_2$ shows significant polarization, as well as high peak current, while the one of β - $\text{Co}(\text{OH})_2$ shows almost no polarization but a lower peak current. Figure 4e, h present the galvanostatic charge-discharge (GCD) curves of these two typical samples at current densities of 1, 2, 4, 8, 16 Ag⁻¹. The sample prepared at -0.9 V (α - $\text{Co}(\text{OH})_2$) exhibits specific capacities as high as 814 and 593 Fg⁻¹ at current densities of 1 and 16 Ag⁻¹, respectively, while 486 and 326 Fg⁻¹ for the sample prepared at -1.5 V (predominantly β - $\text{Co}(\text{OH})_2$). The GCD curves of α - $\text{Co}(\text{OH})_2$ exhibits obvious voltage platforms, while β - $\text{Co}(\text{OH})_2$ does not. These differences in electrochemical behaviors arise from their different crystal structures. α - $\text{Co}(\text{OH})_2$ contains water molecules in the interlayer, which not only maintain the larger interlayer spacing but also facilitate the diffusion of charge carriers. As a results, the electrochemical reaction occurs in the bulk for α - $\text{Co}(\text{OH})_2$, leading to a high specific capacitance and battery-type behaviors, i.e., noticeable polarization in the CV curves and voltage platform in the GCD curves. In contrast, β - $\text{Co}(\text{OH})_2$ lacks water

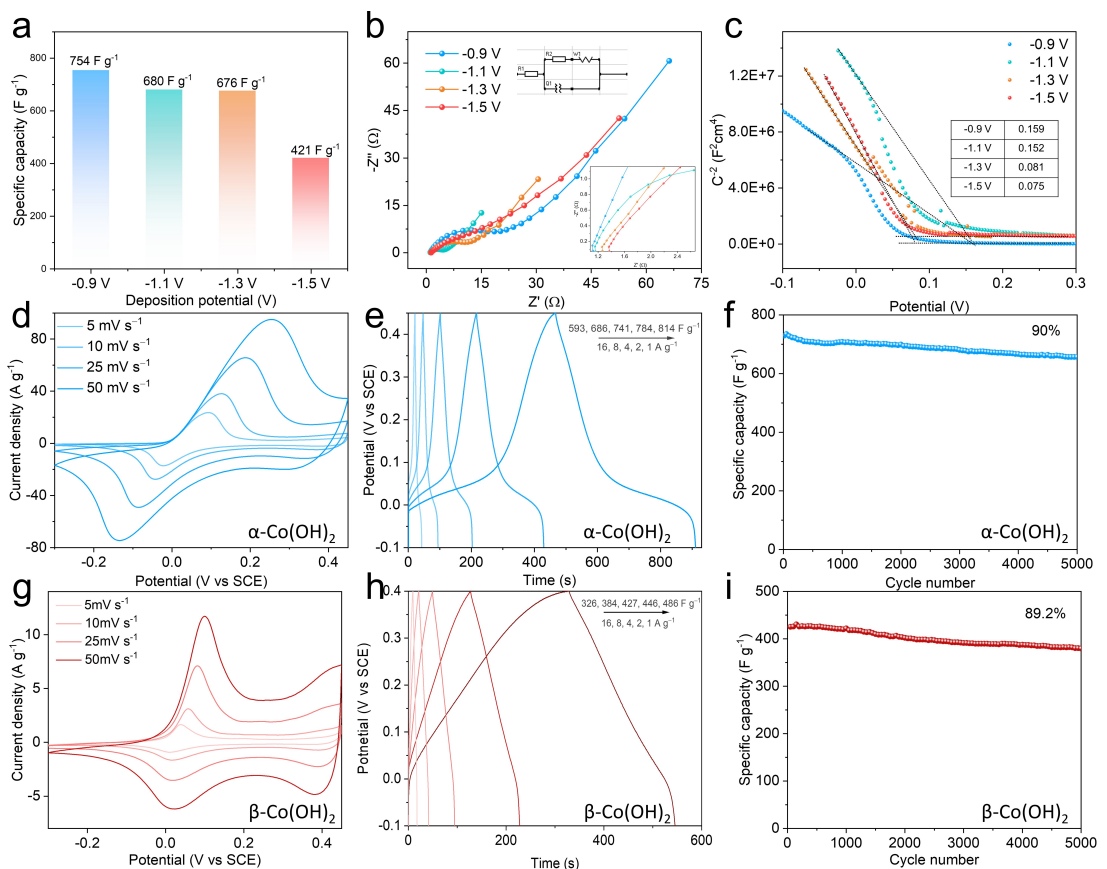


Figure 4. Electrochemical measurements. a) Specific capacity of the electrodeposited samples with different potentials. b) Nyquist plots. c) Mott-Schottky plots. d-f) CV curves, GCD curves, and cyclic stability for $\alpha\text{-Co(OH)}_2$, respectively. g-i) CV curves, GCD curves, and cyclic stability for $\beta\text{-Co(OH)}_2$, respectively.

molecules in the interlayer, and its interlayer spacing reduces to $\sim 4.6 \text{ \AA}$, nearly half of that in $\alpha\text{-Co(OH)}_2$. The small interlayer spacing, coupled with the absence of water molecules, confines the electrochemical reactions to the surface or sub-surfaces of the nanosheets. This results in lower electrochemical performance and a capacitive-type behaviors, i.e., negligible polarization and no voltage platform. Long-cycle stability was evaluated at a current density of 4 A g^{-1} (Figure 4f, i), revealing that the capacity retention rate for $\alpha\text{-Co(OH)}_2$ remains at 90% after 5000 cycles, superior to that of the $\beta\text{-Co(OH)}_2$. Furthermore, we have constructed asymmetric supercapacitor. As depicted in Figure S7, Co(OH)₂ serves as the cathode electrode, while activated carbon acts as the anode electrode. The assembled device exhibits a broad operating voltage window of 1.6 V in 1 M KOH. The $\alpha\text{-Co(OH)}_2$ -based supercapacitor exhibits energy density of 60.5 Wh kg^{-1} at the power density of 181.5 W kg^{-1} . The $\beta\text{-Co(OH)}_2$ -based supercapacitor exhibits energy density of 58.5 Wh kg^{-1} at the power density of 191.4 W kg^{-1} .

The observed discrepancy in electrochemical performance may be attributed to the structural factors discussed above, including the larger interlayer spacing, reduced thickness, and lower crystallinity of $\alpha\text{-Co(OH)}_2$ compared to its β -counterpart. Furthermore, electrochemical impedance spectroscopy (EIS) is employed to investigate the electrochemical kinetics. As illustrated in Figure 4b, the equivalent circuit diagram is also provided by fitting Nyquist plots (inset of Figure 4b, Table S1). The charge transfer impedance

(R_s) can be recorded as follows: $R_{s,-0.9 \text{ V}} < R_{s,-1.1 \text{ V}} < R_{s,-1.3 \text{ V}} < R_{s,-1.5 \text{ V}}$. This suggests that the Co(OH)₂ prepared at -0.9 V possess higher electron conductivity. Co(OH)₂ is a typical semiconductor, and Mott-Schottky (M-S) tests were conducted to ascertain the flat band voltage (E_{fb}), which can be used to determine the valence band value (E_v). As illustrated in Figure 4c, the negative slope indicates that all samples are P-type semiconductors. The E_{fb} values for Co(OH)₂ deposited at different potentials are shown in the inset. The E_v of the samples can be calculated to be -5.64 eV , -5.63 eV , -5.56 eV , and -5.55 eV for samples electrodeposited at -0.9 V , -1.1 V , -1.3 V , and -1.5 V , respectively.^[49]

4. Conclusions

In this work, we systematically investigated the effect of electrodeposition potentials on the phase of Co(OH)₂. We found that the electrodeposition potential can be used to modulate the phase of Co(OH)₂ from $\alpha\text{-Co(OH)}_2$ to $\beta\text{-Co(OH)}_2$ (not phase-pure). The crystal and electronic structure of these two samples, i.e., the sample electrodeposited at -0.9 V ($\alpha\text{-Co(OH)}_2$) and -1.5 V (predominantly $\beta\text{-Co(OH)}_2$), were examined. These analyses reveal significant distinctions in both crystal structure and electronic structure, which correlate with their electrochemical performance. Most importantly, TEM images along the crystal direction $<100>$ were captured by

virtue of a delicate embedding and sectioning techniques, and for the first time, the large interlayer spacing is determined to be $\sim 7.0 \text{ \AA}$ by TEM. We expect our results to enhance the understanding of the preparation and structure Co(OH)_2 . In this regard, future investigations should be focused on the mechanisms that enable the formation of $\beta\text{-Co(OH)}_2$ at reduced electrodeposition potentials, as well as the strategies to inhibit the formation of $\alpha\text{-Co(OH)}_2$ under the same conditions.

Acknowledgements

This work is supported by the National Natural Science Foundation of China (51932003, 52272209). The Beijing Synchrotron Radiation Facility (BSRF) is acknowledged for providing us with beamtime on beamline 4B9 A for XAS measurements.

Conflict of Interests

The authors declare no conflict of interest.

Data Availability Statement

The data that support the findings of this study are available in the supplementary material of this article.

Keywords: $\alpha\text{-Co(OH)}_2$ • Electrode • Electrodeposition • $\beta\text{-Co(OH)}_2$ • Transmission electron microscopy

- [1] T. Dong, W. Yi, T. Deng, T. Qin, X. Chu, H. Yang, L. Zheng, S. J. Yoo, J.-G. Kim, Z. Wang, Y. Wang, W. Zhang, W. Zheng, *Energy Environ. Mater.* **2023**, *6*, e12262.
- [2] P. Gao, Y. Zeng, P. Tang, Z. Wang, J. Yang, A. Hu, J. Liu, *Adv. Funct. Mater.* **2022**, *32*, 2108644.
- [3] Z. Qin, J. Liu, B. Sun, H. Zou, L. Chen, Y. Xu, Y. Cao, C. Chen, *Electrochim. Acta* **2022**, *435*, 141370.
- [4] M. Chen, G. Qu, W. Yang, W. Li, Y. Tang, *Chem. Eng. J.* **2018**, *350*, 209–216.
- [5] C. Wan, Y. Jiao, D. Liang, Y. Wu, J. Li, *Adv. Energy Mater.* **2018**, *8*, 1802388.
- [6] S.-G. Gong, Y.-F. Li, Y. Su, B. Li, G.-D. Yang, X.-L. Wu, J.-P. Zhang, H.-Z. Sun, Y. Li, *Small* **2023**, *19*, 2205936.
- [7] X. Lin, H. Li, F. Musharavati, E. Zalnezhad, S. Bae, B.-Y. Cho, O. K. S. Hui, *RSC Adv.* **2017**, *7*, 46925–46931.
- [8] Y. Tang, Y. Shi, Y. Su, S. Cao, J. Hu, H. Zhou, Y. Sun, Z. Liu, S. Zhang, H. Xue, H. Pang, *Adv. Sci.* **2024**, *11*, 2403802.
- [9] J. Y. Park, H. Y. Kim, Y.-I. Kim, S. Y. Jo, S. A. Abbas, D. Seo, A. Ma, K. M. Nam, *J. Mater. Chem. A* **2022**, *10*, 12047–12054.
- [10] R. Ma, Z. Liu, K. Takada, K. Fukuda, Y. Ebina, Y. Bando, T. Sasaki, *Inorg. Chem.* **2006**, *45*, 3964–3969.
- [11] T. N. Ramesh, M. Rajamathi, P. Vishnu Kamath, *J. Solid State Chem.* **2006**, *179*, 2386–2393.
- [12] W. Zhang, A. Trunschke, R. Schlögl, D. Su, *Angew. Chem. Int. Ed.* **2010**, *49*, 6084–6089.
- [13] A. Hu, Q. Xie, L. Chen, Y. Li, *EnergyChem.* **2024**, *6*, 100137.
- [14] Y. Zhang, X. Xia, J. Kang, J. Tu, *Chin. Sci. Bull.* **2012**, *57*, 4215–4219.
- [15] C. Lai, *J. Alloys Compd.* **2019**, *777*, 492–498.
- [16] Y. Wang, C. Yang, Z. Li, Z. Liang, G. Cao, *Small* **2020**, *16*, 2001973.
- [17] T. Yin, W. Zhang, Y. Yin, Y. Yan, K. Zhan, J. Yang, B. Zhao, *J. Mater. Sci.: Mater. El.* **2017**, *28*, 7884–7891.
- [18] S. Ranganatha, N. Munichandraiah, *ACS Omega* **2018**, *3*, 7955–7961.
- [19] T. Yoshino, N. Baba, *Sol. Energy Mater. Sol. Cells.* **1995**, *39*, 391–397.
- [20] W. Guo, C. Yu, S. Li, X. Song, H. Huang, X. Han, Z. Wang, Z. Liu, J. Yu, X. Tan, J. Qiu, *Adv. Mater.* **2019**, *31*, 1901241.
- [21] R. T. Patil, A. S. Patil, S. D. Dhas, N. B. Wadakar, T. T. Bhosale, V. J. Fulari, *J. Mater. Sci.: Mater. El.* **2023**, *34*, 2297.
- [22] E. M. P. Steinmiller, K.-S. Choi, *Chem. Commun.* **2007**, 159–161.
- [23] J. R. S. Brownson, C. Lévy-Clément, *Phys. Status Solidi* **2008**, *245*, 1785–1791.
- [24] Y.-H. Lee, J. S. Kang, J.-H. Park, J. Kang, I.-R. Jo, Y.-E. Sung, K.-S. Ahn, *Nano Energy* **2020**, *72*, 104720.
- [25] M. Wohlfahrt-Mehrens, R. Oesten, P. Wilde, R. A. Huggins, *Solid State Ionics* **1996**, *86*(88), 841–847.
- [26] F. Wong, R. G. Buchheit, *Prog. Org. Coat.* **2004**, *51*, 91–102.
- [27] D. Steiner Petrović, A. Nagode, D. Mandrino, *JOM* **2020**, *72*, 962–969.
- [28] V. Parra-Elizondo, A. K. Cuentas-Gallegos, B. Escobar-Morales, J. M. Baas-López, J. A. Uribe-Calderón, D. E. Pacheco-Catalán, *Energies* **2019**, *12*, 4246.
- [29] A. Sood, A. D. Poletayev, D. A. Cogswell, P. M. Csernica, J. T. Mefford, D. Fragedakis, M. F. Toney, A. M. Lindenberg, M. Z. Bazant, W. C. Chueh, *Nat. Rev. Mater.* **2021**, *6*, 847–867.
- [30] Q. Feng, C. J. McConville, D. D. Edwards, *J. Am. Ceram. Soc.* **2005**, *88*, 1455–1460.
- [31] H. Suzuki, H. Kurosawa, K. Miyagawa, Y. Hirotsu, M. Era, T. Yamashita, H. Yamane, T. Hirai, *Jpn. J. Appl. Phys.* **1990**, *29*, L1648.
- [32] H. B. Li, M. H. Yu, X. H. Lu, P. Liu, Y. Liang, J. Xiao, Y. X. Tong, G. W. Yang, *ACS Appl. Mater. Interfaces* **2014**, *6*, 745–749.
- [33] D. Wu, Y. Wei, X. Ren, X. Ji, Y. Liu, X. Guo, Z. Liu, A. M. Asiri, Q. Wei, X. Sun, *Adv. Mater.* **2018**, *30*, 1705366.
- [34] S. Liu, R.-T. Gao, M. Sun, Y. Wang, T. Nakajima, X. Liu, W. Zhang, L. Wang, *Appl. Catal. B:Environ.* **2021**, *292*, 120063.
- [35] B. Sun, W. Zheng, S. Lou, B. Xie, C. Cui, G.-X. Zhang, F. Kong, Y. Ma, C. Du, P. Zuo, J. Xie, G. Yin, *Adv. Funct. Mater.* **2023**, *33*, 2211711.
- [36] Y. Su, G. Yuan, J. Hu, G. Zhang, Y. Tang, Y. Chen, Y. Tian, S. Wang, M. Shakouri, H. Pang, *Adv. Mater.* **2024**, *36*, 2406094.
- [37] S. M. Youssry, I. S. El-Hallag, R. Kumar, G. Kawamura, A. Matsuda, M. N. El-Nahass, *J. Electroanal. Chem.* **2020**, *857*, 113728.
- [38] Y. Liu, N. Fu, G. Zhang, M. Xu, W. Lu, L. Zhou, H. Huang, *Adv. Funct. Mater.* **2017**, *27*, 1605307.
- [39] V. Shinde, M. Uthayakumar, R. Karthick, *Surf. Interfaces* **2022**, *32*, 102163.
- [40] T. Shinagawa, N. Kotobuki, A. Ohtaka, *Nanoscale Adv.* **2023**, *5*, 96–105.
- [41] R. S. Jayashree, P. Vishnu Kamath, *J. Mater. Chem.* **1999**, *9*, 961–963.
- [42] J. Li, J.-M. Li, H. Hong, D.-X. Liu, Q.-Q. Cao, D.-H. Wang, *Rare Met.* **2024**, *43*, 289–297.
- [43] J.-P. Sun, Y. Zheng, Z.-S. Zhang, X.-C. Meng, Z.-Z. Li, *Rare Met.* **2024**, *43*, 511–521.
- [44] B. Wang, X. Han, C. Guo, J. Jing, C. Yang, Y. Li, A. Han, D. Wang, J. Liu, *Appl. Catal. B:Environ.* **2021**, *298*, 120580.
- [45] L. Zhang, X. Zhou, S. Chai, J. Guan, G. Fan, W. Yang, G. Ma, N. Han, Y. Chen, *ACS Appl. Nano Mater.* **2022**, *5*, 18680–18690.
- [46] N. P. Dileep, T. V. Vineesh, P. V. Sarma, M. V. Chalil, C. S. Prasad, M. M. Shajumon, *ACS Appl. Energ. Mater.* **2020**, *3*, 1461–1467.
- [47] B. Ravel, M. Newville, *J. Synchrotron Radiat.* **2005**, *12*, 537–41.
- [48] E. Y. Martinez, K. Zhu, C. W. Li, *Inorg. Chem.* **2021**, *60*, 6950–6956.
- [49] X. Chen, Y. Huan, N. Sun, Y. Su, X. Shen, G. Li, J. Zhang, T. Wei, *Chin. Chem. Lett.* **2024**, *35*, 108380.

Manuscript received: November 3, 2024
Revised manuscript received: December 20, 2024
Accepted manuscript online: December 23, 2024
Version of record online: January 8, 2025